The M7 Samos 2020 earthquake: a snapshot of transtension within the Samos - Ikaria Basins

V. Plicka*[1], F. Gallovič[1], J. Zahradník[1], A. Serpetsidaki[3], E. Sokos[3], N. Vavlas[2], and A. Kiratzi[2]

[1] Charles University, Faculty of Mathematics and Physics, Czech Republic

[2] Aristotle University of Thessaloniki, Department of Geophysics, Greece

[3] University of Patras, Department of Geology, Seismological Laboratory, Greece

*Corresponding author: Vladimír Plicka (vp@karel.troja.mff.cuni.cz)

Key points

- Extension on the overriding Aegean plate can cause M7 normal faulting earthquakes
- Source complexity comprises three episodes with a localized coseismic slip of ~1 m at the sea bottom.
- A modern manifestation of a twin-basin evolution (Samos and Ikaria) through active faulting within oblique transtensional regime.

Keywords: Samos, Aegean, rupture directivity, earthquake, slip model, transtension

Abstract

The October 30, 2020, Mw7 Samos earthquake ruptured a north-dipping offshore normal fault, bounding the homonymous basin. Genetically is related to the rapid southward motion of the Aegean, contributing to significant extension and the development of active graben structures within a dextral shear zone. It will be recalled as among the deadliest (118 fatalities) that affected the Greece-Turkey cross border region, generated a strong tsunami, and caused a co-seismic uplift of 20 to 35 cm of the NW part of the Samos Island. Using broadband, strong-motion and geodetic data, we constrain the location and source geometry of the mainshock. A multiple-point source model suggests three sequential subevents providing 20 s of source duration. Our finite-fault kinematic model confirms the prevalence of large slip amplitudes (~2.4 m) along the entire ruptured area and the up-dip and westward rupture propagation. This directivity is independently confirmed by Apparent Source Time Functions inferred from regional recordings using a herein developed empirical Green's function method. Static GNSS displacements from inland stations yield a near-surface co-seismic slip of ~1 m amplitude, breaking the sea bottom and contributing to any interpretation of the observed island uplift. The 2020 Samos event dramatically showed that in the spatially heterogeneous oblique transtentional regions in the back-arc Aegean region, normal faults bounding the basins are capable to rupture in M7 earthquakes, provoke tsunami generation, and constitute a constant threat for the nearby coastal areas of both Greece and Turkey.

Introduction

The characteristics of the faults that rupture during earthquakes in the Aegean Sea and surrounding lands are essential for understanding the driving mechanisms that control the distributed deformation. To this end, the focus of our study is a normal faulting event: the October 30 2020 Samos earthquake of moment magnitude Mw7.0 (GCMT, Dziewonski et al., 1981; Ekström et al., 2012). It occurred ~ 9 km offshore the northern coast of Samos Island in the eastern Aegean Sea (Fig. 1). The broad tectonic setting (Fig. 1 inset) is governed by i) the rapid (~24 mm/y) westwards escape of the Anatolia block towards the Aegean, facilitated by the operation of the dextral strike-slip North Anatolian Fault (NAF), in conjunction with the sinistral strike-slip East Anatolian Fault (EAF) and ii) the even faster (~35 mm/yr) southward retreat of the trench and of the Hellenic subduction zone, which is rolling back towards Africa (Jolivet et al., 2015, Faccenna et al., 2014). As the trench retreats southwards, it pulls the overriding Aegean plate, causing significant north-south extension and thinning of the overlying lithosphere (Karabulut et al., 2019; Le Pichon et al. 2019). The extension is so intense that the Aegean Sea and the surrounding lands rank among the most rapidly extending continental regions worldwide (Meng et al., 2021), resulting in a frequent occurrence of normal faulting earthquakes.

The northern coastline of Samos island (Fig. 1) is bounded by dominant E–W striking normal faults, mainly inferred from sea topography. Soon after the occurrence of the mainshock, the causative fault was identified (Ganas et al., 2020) and associated with the Samos Basin Fault from bathymetry surveys (Nomikou et al., 2021). This fault is also included in the fault databases as Kaystrios Fault (Caputo and Pavlides, 2013) or as North Samos Fault (Chatzipetros et al., 2013). The mainshock predominantly ruptured the western segment of this fault, having no documented historical event (since ~1700). Contrarily, several strong events (e.g., in 1873 and 1893, M~6.5) may be associated with its eastern segment (Kiratzi et al., 2021, and references therein).

Being among the strongest and deadliest events to occur during instrumental times along the Turkey-Greece cross border region, the Samos earthquake attracted the scientific community's attention. Many preliminary reports by various agencies in Turkey and Greece were quickly available (Cetin et al. 2020 and references therein; Papadimitriou et al. 2020; among others). The list of journal publications is continuously augmenting, and we may not exhaustively reference here all of them. Journal special issues were compiled, and the reader can seek more information in Acta Geophysica, summarized by Zúñiga and Tan (2021) and in the special issue of the Bulletin of Earthquake Engineering. For a complete summary of all Samos-related papers, the existing and even future ones, see the International Seismological Centre, On-line Event Bibliography (Di Giacomo et al., 2014).

The specific focus of our work is to search for any source complexity, and assess the characteristics of the rupture history to provide a finite-fault kinematic

model of the mainshock. Because many models are already available, our work is structured as follows: we first discuss the so far available findings and discuss similarities and differences among them, then we present the motivation and the scope of our work, and finally, in a broader context, we discuss the strong earthquake clustering in the broader Aegean Sea region and the surrounding lands.

Key characteristics of the sequence, open issues, and motivation of this work

Life loss, environmental effects, observed tsunami: The Samos earthquake caused 2 fatalities and 19 minor injuries at Samos Island, but 116 deaths and over 1,030 injuries in Izmir (Turkey), a city of ~4M inhabitants (Cetin et al., 2020). The damage in the Izmir Bay area (Bayrakli district), ~70 km away from the epicenter, was mainly attributed to site amplification of ground shaking, at site frequencies in the range 0.7 to 1.6 Hz, for both stiff and soft soil sites (Makra et al., 2021). The mainshock caused a moderate tsunami, which affected nearby Samos Island and cities along the Aegean coast of Turkey, resulting in substantial property losses. The maximum tsunami inundation (i.e., max horizontal intrusion) was 2.31 m, and its maximum runup was 3.82 m (Dogan et al., 2021). The tsunami arrived within ~10 min to the coast of NW Samos Island and within 20 min to the coast of Turkey, and sea recession was the leading motion (Triantafyllou et al., 2021). No consensus has been reached on the tsunami triggering mechanism, whether it was generated by co-seismic seafloor displacement, by earthquake-induced submarine landslides along the fault scarp, or a combination of both. Field reconnaissance measured co-seismic shorelines' uplift of 20±5 to 35±5 cm at the western coastline of northern Samos (Evelpidou et al., 2021). GPS-derived displacements indicated tectonic uplift of almost 10 cm on Samos Island (Ganas et al., 2020). A key issue contributing to the discussion regarding the observed uplift and tsunami generation is to constrain whether the rupture reached the seafloor. These are key parameters to get an idea of the capability of normal faulting earthquakes to generate tsunamis.

Hypocenter location of the mainshock and vertical distribution of the aftershocks: In the aftermath of the mainshock, initial relocations were available, based on published P- and S-wave arrivals at stations located in Greece and Turkey (Papadimitriou et al. 2020; Foumelis et al., 2021). Subsequently, many groups provided relocated aftershock catalogs (Karakostas et al. 2021; Kiratzi et al. 2021; Lentas et al. 2021). The main difference among the results is the depth of the mainshock and the depth extent of the sequence. Karakostas et al. (2021) calculated the depth at 16.88 km and the aftershocks located at depths mainly between 10 to 15 km. Whereas the other two groups (Kiratzi et al. 2021; Lentas et al. 2021) converge on shallower depth for the mainshock (8 to 10 km) and predominant spread of the aftershocks at shallow depths, in the range 5 to 10 km, in agreement with the results of this work.

Identification of the fault plane - dip angle variability: The nearly E-W striking, north-dipping nodal plane has been identified as the fault plane, based on geodetic data (Ganas et al., 2020) and seismic data (Papadimitriou et al., 2020; Karakostas et al., 2021; Taymaz et al., 2022; Kiratzi et al., 2021, and references therein). This agreement among researchers is significant, compared to the disagreement on the dip direction of other normal faults, such as the one of the 2017 Kos-Bodrum Mw6.6 earthquake in the Gulf of Gökova (Kiratzi and Koskosidi 2018; Konca et al., 2019 and references therein). Despite the agreement on the northward dip of the fault, the value of the dip angle was rather variable (see Table 2). It ranged from as shallow as 29° (USGS), 37° (GCMT) to as steep as 55° (KOERI). Normal faults with dips lower than ~40° have not been observed within the overriding Aegean plate, warranting careful analysis.

Source complexity, slip distribution models, inferred westward rupture propagation: Even though finite-fault slip models have already been published, a systematic search for source complexity and the presence of any subevents has not been performed. Complexity can only be inferred from the number and location of slip patches (asperities). The comparative characteristics of the, so far, published slip models depend on the inversion scheme, data, fault model parameterization, accuracy of the Green's functions, the frequency band used, among other parameters. Based mainly on teleseismic data and only two strong motion components, the model by Karakostas et al. (2021) shows a small peak slip amplitude (~1m) and a deeply rooted slip patch (at ~25 km), which differs from other models based on similar data (Chousianitis and Konca, 2021). The model by Kiratzi et al. (2021), based on regional seismic data in a frequency band between 0.02 and 0.08 Hz, indicates: a) slip confined in an area 32 km ×15 km, and at very shallow depths less than ~10 km; b) peak slip amplitude of ~3.5m, situated ~18 km to the west of the hypocenter, c) top of the fault at 0.5 km, nearly reaching the seafloor and d) a dominant up-dip and westward rupture propagation. The kinematic rupture inversion of Lentas et al. (2021) is based on local strong motion data, adopting fault geometry, slip direction and seismic moment from the GCMT solution without further optimization. Their results suggest a non-uniform bilateral rupture on a 60 km × 20 km fault, with the main rupture propagating towards the west and maximum slip of ~2.5 m. Chousianitis and Konca (2021) jointly inverted geodetic (static GPS offsets and high-rate waveforms), teleseismic and strong-motion data, filtered between 0.02 and 0.4 Hz. Their preferred model is dominated by a slip patch 30 km × 10 km, along strike and dip, respectively. Taymaz et al. (2022) using back-projection and kinematic and dynamic finite-fault modeling of seismic data, obtained a rupture of 50 km x 20 km with two main asperities and maximum slip of 3.2 m.

To sum up, the so-far published models are quite variable, specifically regarding the peak slip amplitude and the spatial distribution of the slip patches along strike and depth. These issues are crucial to interpret the damage pattern and provide valuable input to the modelers if the observed tsunami could relate to sufficient seafloor dislocation.

Scope of the present work

To alleviate the variability of the published results we reanalyze the earthquake using a dataset consisting of broadband (BB) and strong motion (SM) digital recordings and GNSS static displacements. Our workflow is as follows:

a) relocation of the mainshock hypocenter and of the aftershock cloud to re-assess the spatial and vertical distribution of the sequence, benchmarking the consistency of available velocity models;

b) multiple-point source modeling to assess the fault geometry, especially the dip angle of the fault plane, and search for source complexity in variable frequency bands;

c) finite–fault kinematic slip inversion including optimization of the fault geometry and slip direction to constrain the spatial and vertical distribution of the slip, including its peak amplitude and how close to the seafloor the rupture propagated;

d) inference of the rupture directivity by inspection of the finite-extent source slip model and apparent source time functions (ASTF) retrieved by a new Empirical Green's Function (EGF) method, originally developed in this paper. Note that the ASTF-EGF analysis was missing in the previous publications about the Samos earthquake.

e) synthesis of the results within the regional seismotectonic context.

Hypocenter locations and basic parameters

Mainshock hypocenter location

We manually picked P- and S-wave arrivals from strong-motion (SM) and broadband (BB) stations, 81 in total, at epicentral distances from 20 to 290 km (Fig. S1). Several 1-D velocity models (VM) applicable to the region are available, which allowed us to benchmark their efficacy to provide consistent results regarding the mainshock hypocenter and get an estimate of the uncertainties. We examined 8 velocity models and located the mainshock using the probabilistic NonLinLoc code of Lomax et al., 2000 (see Section 1A, and Figs S1, S2 in the Supplement for details). The location of the epicenter is very stable, at 37.900°N and 26.817°E (±2.5 km) within all the models tested (Fig. 2 and Table 1). Although the depth is generally the most challenging parameter to constrain, all models indicate hypocenter depths in the upper crust, at ~12 km and shallower. The models of Konstantinou (2018) and Novotný et al. (2001) provide comparable P- and S- residuals ~±1s at all epicentral distances (Fig. S2). The model of Novotný et al. (2001), derived from surface-waves dispersion, has proven to be very efficient in describing wave propagation in the Aegean area, especially at low frequencies used in the finite-fault modeling.

Relocation of aftershocks

The manually picked events recorded during the first 40 days, initially located with Hypoinverse (Supplement B), were relocated with HypoDD (Waldhauser and Ellsworth 2000; Waldhauser 2001). Among all the velocity models examined regarding their location uncertainties and their hypocenter distribution (see Section 1B and Figs S3 to S6 in the Supplement for details), the Özer et al. (2018) was adopted as the most appropriate. This model was derived from the most recent seismic experiment in the study area and provided the best travel-time data fit and better hypocenter distributions without artificial linear depth concentrations. Figure 3 summarizes the final relocated dataset of ~1300 events in total. The aftershock's spatial distribution indicates that the area just west of the hypocenter is depleted in aftershock productivity compared to the nearby eastern region (see also Figs. S6 in the Supplement). This observation is a first proxy for the inferred locus of the major slip, later confirmed by our slip model. The aftershocks tend to distribute in four clusters. The cross-sections (Fig. 3 top panels) depict that: i) the sequence evolved in the upper crust (h $<$ 15 km) and the aftershocks are mostly up-dip from the hypocenter ii) the causative fault dips to the north, and iii) secondary structures were activated. The main cluster comprising the mainshock's hypocenter borders the Samos northern coastline, and all aftershock mechanisms associated with it depict pure normal faulting along E-W striking planes (Karakostas et al., 2021). The cluster formed west of the main one (cross-section C1C2, Fig.3) can be considered the westernmost part of the main causative fault, dipping slightly steeper than the main one to the NNE and indicating normal faulting as well. The westernmost cluster (cross-section B1B2, Fig.3) represents a NE-SW alignment following the Ikaria basin topography (Nomikou et al., 2021). The easternmost cluster (cross-section A1A2, Fig.3), inland Samos Island, shows a fault dipping steeply, almost vertically. These secondary structures can be associated with focal mechanisms that exhibit strike-slip motions (Karakostas et al., 2021, Fig.3). The aftershocks distribution suggests that strike-slip faults border the main activity area.

Multiple point source (MPS) modeling of the mainshock

Before proceeding to finite-fault modeling, we investigate the source process of the mainshock using the multiple-point source modeling tool available in the ISOLA software package (Zahradník and Sokos 2018; Liu and Zahradník, 2020, and references therein). We describe the rupture process as a sequence of points of moment release episodes, known as subevents. This is an approximate representation of the continuous source process. It depends on epicentral distances and frequency range, visualizing the same source either as a point at low frequencies or a series of points at higher frequencies. We adopt the velocity structure of Novotný et al. (2001) to calculate full-waveform synthetics.

We started with the employment of waveforms from BB stations in the epicentral distance range of 263 to 456 km and their centroid moment tensor (CMT) inversion in the frequency range between F*min* of 0.005 Hz and F*max* varied as 0.02, 0.03, and 0.04 Hz. The minimum and maximum frequencies are constrained by noise (natural and instrumental) and the accuracy of the velocity model, respectively. For the lowest F*max* value, we found a poor spatial resolution of centroid and a slightly overestimated moment magnitude (Mw = 7.04, compared to Mw = 7 of GCMT). For the other values of F*max* we obtained Mw =7.0 and 6.9, respectively, with satisfactory waveform fit (variance reduction VR = 0.8 and 0.6), and a consistent position of the centroid, shifted 20-km westward of the epicenter, and with the centroid time ~10 s relative to origin time. The latter can be taken as a proxy of the source half-duration, as later confirmed by more detailed modeling. The optimal centroid depth was between 6 and 8 km, representing an improvement compared to the artificially fixed 12 km depth of GCMT. Besides, we found the centroid depth almost independent of the used velocity model, being significantly more stable than the hypocenter depth. Regarding the focal mechanism, we found a stable, high-percentage double-couple deviatoric source (DC > 85%), with strike/dip/rake (s/d/r) angles equal to 270°/50°/-100°, slip vector azimuth/plunge = 15°/49°, which is close to the GCMT solution (Table 2), as demonstrated in Figure 4.

Employing SM stations in the distance range 30 to 155 km and frequency range from 0.04 to 0.09 Hz, the earthquake appears as a multiple point source. To stabilize the inversion, we kept the depth fixed at 6 km and searched for best-fitting positions of point sources along an E-W striking horizontal line. Using the double-couple constrained inversion, we identified three relatively stable subevents, shown in Figure 4, alongside our subsequently discussed slip model. The subevents' focal mechanisms denote predominant normal faulting. A cumulative tensor sum of the subevents' MTs yields an effective point-source mechanism with s/d/r equal to 246°/44°/-125°, slip vector azimuth/plunge = 20°/35°, being close to the GCMT solution (Kagan angle 21°), Mw = 7.0 and VR = 0.63. Considering also a possible fourth subevent, we found it unstable and providing only negligible improvement to the waveform fit. For example, our models with one, two, or three subevents featured VR ~ 0.33, 0.57, 0.63, while the fourth subevent increases VR just to 0.67, That is why we prefer a 3-point model.

We intentionally do not go into more specific details; changing any parameter, e.g., F*max*, or removing any single station, the results are obviously changing. It is a matter of expert judgement to recognize gross features of the MPS model that we present here as follows. The first subevent is situated ~4 km east of the epicenter, indicating an initial eastward rupture propagation. The other two subevents, located at ~12 and ~32 km west from the epicenter, support the predominant westward propagation, further confirmed by our modeling. The focal mechanism of the subevents in Figure 4, expressed with s/d/r, is as follows: sub1 271°/46°/-106°, sub2 225°/40°/-155°, sub3 249°/54°/-110°. The subevents occur at ~6, ~10, and ~15 s after origin time, providing ~20 s of the total source duration. This agrees with the source time function inferred by Geoscope, us-

ing the SCARDEC method (Vallée et al., 2011). Using the subevents' source mechanisms and the non-negative-least squares (NNLS) method of Lawson and Hanson (1974), we calculated the moment rate function (MRF); for the technique, see appendix of Zahradník and Sokos (2014). This MRF is compared with the one obtained from the slip inversion model (Fig. 4). Both functions depict a total source duration of ~ 20 s. The agreement with teleseismic studies of GCMT and SCARDEC guarantees that our analysis of regional data is not biased.

Finite-Fault kinematic rupture model

We used the Linear Slip Inversion (LinSlipInv) method of Gallovič et al. (2015) to infer kinematic finite-fault description of the rupture process, a technique applied to many previous earthquakes in Greece (Sokos et al., 2015, 2016, 2020). Table 3 lists the quantities describing the setting of the calculation. In LSI, slip rate functions, spanning the entire rupture duration, are discretized in time and space. Synthetic Green's functions are calculated by the discrete wavenumber method adopting the Novotný et al. (2001) crustal model (as in ISOLA analysis) in frequency range 0.02 to 0.15 Hz. At higher frequencies, the details of the source and wave propagation in the medium (e.g., effects due to local heterogeneities) could not be adequately captured by the 1D velocity model. The data are displacement waveforms acquired from local strong motion stations (Fig. 4) filtered in the same way as the Green's functions, using the 4th order causal (single-pass) Butterworth filter. We also employ static GNSS data adopted from Ganas et al. (2021).

We stabilize the inverse problem by i) assuming prior covariance function with k^{-2} decay at large wavenumbers k, ii) prescribing seismic moment inferred by the CMT inversion using ISOLA modules, and iii) positivity of the slip rates. Regarding the latter, we use the NNLS approach of Lawson and Hanson (1974). We point out that the source description in the LSI method is very general, with no prior constraints on the position of the nucleation point, rupture speed, and shape of slip-rate functions. A drawback of this loose parameterization is that the result is sensitive to artifacts and biases imposed by the imperfect station distribution and smoothing (Gallovič and Zahradník, 2011; Zahradník and Gallovič, 2010). To this end, the result must be carefully interpreted considering lessons learned from previous synthetic tests and real-data applications (Gallovič, 2016; Gallovič et al., 2015).

The fault is modeled as a rectangle, 100 km × 24 km along strike and dip, respectively. We grid-searched its position and mechanism: strike (240°, 250°, 260°, 265°, 270°), dip (35°, 40°, 45°) and rake (-100°, -110°, -120°, -130°), position in the north-south direction was varied by ±5 km with respect to the centroid. The best waveform fit (waveform variance reduction VR = 0.618 and GNSS VR = 0.978, see Fig. 5) and the least artifacts occurrence were attained for the initial fault position (with its center fixed in the centroid) and for strike/dip/rake

= 265°/40°/–110°.

The preferred slip model (Fig. 4) shows that the main slip episode occurred west of the epicenter. The slip is located both at depth, but also close to the surface. We point out that the shallow slip is illuminated almost exclusively by the GNSS data. Indeed, if the GNSS data are neglected in the inversion, the surface slip is not revealed, while the closest GNSS is underestimated by about 50% (see Fig. S7). Noting that the waveform improves only slightly when GNSS data are omitted (VR = 0.623), the seismic data proves insensitive to the temporal evolution of the shallow slip, at least in our frequency range and with our station coverage.

Snapshots of the inferred slip rates (Fig. 5) suggest that the rupture started close to the epicenter (not *a priori* prescribed in the inversion). On the dipping fault, the hypocenter lies at 6 km depth. The rupture propagates bilaterally mainly up-dip for the initial ~3 to 4 s (see the analogy with the first subevent of the MPS inversion delayed by 6 s after the origin in Fig. 4a, and the slip-rate peaks at 4 to 8 s in the LSI snapshots of Fig. 5b). After that, the rupture continues to the west, i.e., towards mainland Greece, creating the major slip within 8 to 16 s after the origin time, extending ~40 km westwards of the hypocenter and to shallow depths (see the second and third subevent in the MPS model and the dominant slip patches in the EGF and LSI models).

The ruptured area extents 60 km along strike and 20 km along dip. The peak slip reaches 2.4 m. It is thus similar to Lentas et al. (2021), who used the same inversion method but without optimizing the fault geometry and slip direction and employing only the seismic data. The other published models are characterized by smaller rupture areas (and thus larger peak slip), which might be related to the strength of the smoothing constraint in the individual applications. Indeed, comparing slip distribution inferred by the kinematic (Pizzi et al., 2017) and dynamic (Gallovič et al., 2019) rupture inversions for the 2016 Amatrice earthquake, the latter resulted in ~1/3 times smaller rupture length. Since the Amatrice application utilized stations at shorter distances than in the Samos earthquake, the true rupture extent of Samos might be between 30 and 40 km. A similar estimate would be obtained, if the rupture area is defined assuming a contour of ~0.5 to 0.8 m of minimum slip.

As mentioned above, the shallow slip is constrained just by the GNSS data with almost no effect on the waveform fit (Fig. S7). Therefore, we consider the temporal evolution of the surface rupture as poorly constrained. We hypothesize that the rupture had a relatively long slip rate duration at shallow depths due to long rise times and/or slow rupture propagation, with small slip-rate peaks and thus weak radiation of seismic waves, especially at periods dominating the displacement waveforms (~10 to 20 s).

For our kinematic model parameterization, the rupture speed can be only roughly estimated, keeping in mind that only a very smoothed image has been revealed (Gallovič et al., 2015). For the dominant westward faulting, the speed

can be estimated from the slip-rate peak position at 45 km along strike at 8 s and the termination of the rupture 8 s later occurring at about 70 km (see the snapshots in Fig. 5). This suggests a relatively high rupture speed of about 3 km/s. Obviously, we cannot rule out the possibility that the rupture could have propagated slower/faster or more episodically during each moment release episode.

Apparent Source Time Functions (ASTFs)

Rupture directivity is a key element of the physics of earthquakes, and here we seek to explore this feature employing the empirical Green's functions (EGF) approach. Several methods were developed to obtain ASTF (e.g., Mueller, 1985; Mori and Hartzell, 1990; Bertero et al., 1997; Courboulex et al., 1999; McGuire, 2004; Vallée, 2004; Roumelioti et al., 2009; López-Comino and Cesca, 2018). Most of them are based on spectral deconvolution, requiring careful stabilization. Here we suggest a simple new alternative technique based on the NNLS technique, fully operating in the time domain, assuming that the ASTF is implicitly positive and seismic moment is constant across the stations (see supporting Section 3 and Figs. S8-S12).

We calculate apparent source time functions (ASTFs) from regional waveform data by the NNLS technique (see supporting Section 3 and Figs. S8-S12) and investigate their duration and amplitude variation with azimuth. This method only requires finding an aftershock to serve as an empirical EGF, originating at a similar depth and location with the mainshock and having a similar focal mechanism. No further assumptions are made (no source or velocity model is needed). The aftershock sequence was depleted in strong aftershocks, specifically in the suitable magnitude range M5 to M6. This significantly narrowed the number of suitable EGF's. Exploiting the available data, we finally selected two aftershocks (Event1, M5 of October 31, 2020, 05:31 UTC, and Event 2, M5.1 of October 30, 2020, 15:14). The waveform similarity supports the similar focal mechanisms of the selected EGFs (Cetin et al., 2020) and the mainshock. For these two events, we obtain two ASTFs. The ASTFs are searched in a time interval from -5 s to 35 s relative to origin time, i.e., in the 40 s time window. We invert the full seismogram at each station, including P and S waves and all three components. We have also calculated ASTFs using the P or S waves groups only, but the results were similar to the inversion of complete records. The frequency band of inversion was chosen at 0.05 to 0.5 Hz, but higher frequencies can also be used. We have inverted the original acceleration, velocity, or integrated records, and the results were stable.

ASTFs obtained from events 1 and 2 are very similar at all stations (Fig. 6a). Such similarity indicates the inversion stability and good selection of both events as an EGF. The inferred ASTFs (Fig. 6) from stations located orthogonal to the fault strike (EFSA, PRK, SOMA, TVSB in the north, and KLNA, ASTA, ARG in the south) depict longer pulse duration and lower amplitudes, compared to

those located along strike (KARY, VLY, TNSA in Greece and NAZL in Turkey), supporting westward rupture propagation. More specifically, NAZL lies in the backward direction of rupture propagation, whereas KARY, VLY, and TNSA are in the forward direction, exhibiting narrow, high-amplitude pulses.

Assuming a horizontal rupture propagation featuring a unilateral rupture propagation on a part of the fault, apparent duration $\tau(f)$ as a function of station azimuth f can be described by

$$\tau(f) = T_1 + T_2 \left(1 - \frac{V_r}{V_{P,S}} \cos(f - \alpha)\right) = T_D - \frac{L_2}{V_{P,S}} \cos(f - \alpha). \quad (1)$$

Here $T_D = T_1 + T_2$ is the total rupture duration, T_1 is the rupture duration corresponding to the nondirective part of the fault, and $T_2 = L_2/V_R$ is the rupture duration of the fault portion L_2 with assumed unilateral rupture propagation at the speed V_R. The $V_{P,S}$ is the velocity of P or S waves, and α is the rupture directivity azimuth.

We have tested several combinations of T_D and $\frac{L_2}{V_{P,S}}$ to find the optimum ones that provide the best match with the observed duration of the ASTFs (Figure 6b). The direction of rupture α = N265 $^\circ$ is fixed, obtained from our fault slip model. The best fit to the data is for values: T_D= 22 s $\pm$2 s, $\frac{L_2}{V_{P,S}} = 7\ s$ (curve in Figure 6b). If we consider the S-wave velocity in the source depth (e. g., V_s = 3.5 km/s in the Novotný et al. (2001) model), the length of the directive zone is L_2 = 24.5 km, which corresponds to the estimate from the kinematic finite-fault modeling. We note that the rupture velocity V_R cannot be inferred from the durations of the ASTFs (Eq. 1).

Discussion

The Samos earthquake within the broader tectonic context

The Aegean Sea is a nice example of a geometric organization of fault structures as relics of the superposition of different deformation phases through geologic time scales. First of all, a consensus has been reached, that the present-day kinematics indicates that the ongoing extension of the overriding Aegean plate can be attributed to both the southward trench retreat and the westward displacement (or escape) of Anatolia along the North Anatolian Fault (NAF). On the other hand, the geological and stratigraphic record indicates that this interaction initiated in the middle Miocene, while ~10My later, in Late Miocene to Pliocene (Sengor et al., 2005) or Pliocene-Pleistocene (Philippon et al., 2012), the NAF propagated westward and entered the Aegean. Moreover, since the middle Miocene, the trench retreat accelerated to become 3.2 cm/y during the last 13 My (Brun et al., 2016). In this framework, from the middle Miocene to nowadays, the Aegean crust has been subjected to distributed extension, which facilitated the widespread formation of offshore and onshore Neogene sedimentary basins, in a dextral transtensional regime (Sakellariou et al., 2013; Beniest

et al., 2016).

Figure 7 summarizes how the present-day crustal deformation in the Aegean Sea is accommodated by, or partitioned among, a regional network of faults with different orientations, and how this apparent complexity is depicted by the diversity of earthquake mechanisms. In general, structures sub-parallel to the displacement field (relative plate-motion) vectors exhibit shear motions (dextral strike-slip faulting) whereas structures oblique to these vectors exhibit an additional extensional motion, producing a combination of dip-slip and strike-slip mechanisms. The dextral strike-slip motions terminate at the edge of continental Greece along an NW-SE trending zone, which is an orientation of structures imposed from past deformational phases, and the sense of motion is sinistral strike-slip. Additionally, it is notable that the strike-slip motions diminish as we move south, where the extension is dominant, as we are closer to the subduction zone, and the effect of trench retreat is more pronounced.

Our main result in Figure 8 is the interpretation of the Samos earthquake in terms of an evolution of two basins (Ikaria and Samos) through active seismic faulting in the modern transtensional tectonic regime that originally formed during the initiation of dextral transtension in the central Aegean. More specifically, it is evident that the basins north of Ikaria and Samos islands, constitute two depocentres, and, due to their proximity, should be jointly examined. The Ikaria Basin is the second deepest (1400 m maximum water depth) basin in the Aegean Sea, after the North Aegean Trough. Its geometry is rather symmetric and somewhat circular, contrary to the nearby Samos Basin, which is highly asymmetric and considerably shallower (Nomikou et al., 2021). The Samos mainshock is a modern episode of basin evolution through active faulting, as sketched (Fig. 8).

Specific elements of the Samos earthquake

What has this normal faulting event added to previous knowledge? It offered evidence for the considerable amount of crustal (and lithospheric) stretching occurring in the back-arc Aegean Sea area. The geometry of the fault confirms worldwide findings for normal faulting. Thirty years ago, it was summarized by Jackson (1987): "*Large normal-faulting earthquakes on the continents show that the overwhelming majority of such earthquakes nucleate in the depth range 6-15 km on faults dipping between 30° and 60°*". The nucleation depth and the resolved dip angle of the Samos earthquake are compatible with this generalization. Gross features of seismic waveforms and GNSS data could be explained with a planar fault. However, we should bear in mind that this is still just a simplified model, reflecting the current density of the observing networks. For example, the multiple point-source modeling indicated a possibly varying focal mechanism during the event, but we do not possess enough data to resolve such complexity. Equally limited is our ability to exactly constrain fault geometry by aftershock relocation because existing velocity models are inadequately detailed for a particular local study. Nevertheless, compared to the state of the art 30

years ago, thanks to instrumental and modeling progress, this study (and other parallel studies of the Samos earthquake) reveals important particular details and provides certain methodical implications, as follows.

We explored rupture directivity based on the Apparent Source Time Functions (ASTFs) obtained from regional strong-motion and broadband seismograms, a technique that has not been applied to this event so far, and importantly complements the slip inversions limited by inaccuracies of existing velocity models (and synthetic Green's functions). The ASTFs, in the along strike and orthogonal to the fault directions, demonstrated pronounced variation in amplitudes and durations, implying directivity to the west. Globally, the along-strike directivity of normal faults has been so-far relatively rarely reported (Calderoni et al., 2015; Pacor et al., 2016). This event thus contributed to the database of such faults in the Eastern Mediterranean.

Additionally, the Samos earthquake generated a tsunami with strong waves of ~3.35 m height inundating the town, 2min and 4min after the origin time (site K4 in Triantafyllou et al., 2021). Whether the runup was generated by co-seismic seafloor displacement, by a triggered submarine landslide, or by a combination of both, is a matter of debate. Our slip model indicates 1.1 m slip reaching the sea bottom, offshore the Karlovasi town. The temporal resolution of this shallow slip patch is poor due to the insensitivity of the seismic waveforms, suggesting rather long rise times and/or slow rupture propagation at the shallow depths. Nevertheless, this inference may constrain tsunami modeling.

The Samos earthquake as another signal of localized deformation

The Samos earthquake adds new evidence on the concentration of the deformation signals along the boundaries of the Aegean plate, as manifested by a cascade of ongoing strong events during the last 15 years or so. Since 2006, 27 strong (M 6) earthquakes occurred in the Aegean Sea and the surrounding lands (Fig. 9). Most of these events are shallow and have epicenters that remarkably bound the Aegean Plate, while a few occurred within the subducting African lithosphere (depth $>$ 60 km; magenta colors in Fig. 9). Remarkably, all types of deformation are exposed to operate simultaneously, as reflected in the focal mechanisms within this short period: The Africa-Aegean collision, the presence of a subducting plate, the shear motions at the boundaries of the plate, the distributed extension along the overriding plate. In this way, seismology is providing improving constraints for new types of high-resolution geodynamic models of the plate interactions.

Within four years (2017 to 2021), the sequential occurrence of normal faulting earthquakes at graben structures, close to coastal western Anatolia events (2017 Lesvos Basin; 2017 Kos-Bodrum Gökova Basin; 2020 Samos Basin) and on the Greek mainland (2021 Thessaly Basin) reflects the intense ~N-S stretching of the upper Aegean Sea plate. Improved seismic networks permitted monitoring

of many swarms that occurred along the cross-border region. For example, in Gökova basin in 2004 and 2005, in Biga Peninsula in 2017, the currently operating close to the Nisiros volcanic island, pointing to an increased level of localized stresses across the region. This localization and tectonic diversity (complexity) mentioned in the previous paragraph represent a challenge for seismic hazard assessment. Although the Samos earthquake ruptured a known fault, future events nearby may have a different focal mechanism. It calls for a new generation of fault databases including uncertainties.

Conclusions

We used broadband and strong-motion waveforms, together with geodetic data, to explore source complexity, finite-fault kinematic modeling, and rupture directivity. We carefully searched for stable features of modeling results by filtering the data at discrete and variable frequency ranges, using all the data and/or selected subsets. Our results can be summarized as follows:

- Our relocation confirms hypocenter depth in the range from 6 to 12 km (not deeper). We constrain the epicenter with an uncertainty of $\pm$2.5 km, using six existing velocity models. Our relocated aftershocks suggest that the sequence deployed at shallow depths (h $<$ 15km) in the brittle upper crust.

- Although we do not prescribe the hypocenter *a priori*, the resulting space-time history of slip points to nucleation at a depth of 6 km, further narrowing the depth uncertainty.

- We optimized the fault geometry and slip direction during our kinematic finite–fault slip inversion. The best strike/dip/rake values are 265°/40°/-110°, corresponding to an E-W striking normal fault, moderately (40°) dipping to the north, with predominantly normal slip component.

- Multiple point source modeling, finite-fault kinematic slip inversion, and analysis of Apparent Source Time Functions (ASTFs) suggest the following rupture evolution scenario. The rupture initially propagated eastward or bilaterally during the first ~7s to at least 5 km east of the epicenter. Then the rupture propagated unilaterally to the west for at least 30 km of the epicenter for another ~10 s. Globally, the along-strike directivity of normal faults has been so-far relatively rarely reported (Calderoni et al., 2015; Pacor et al., 2016). This event thus contributed to the database of such faults in the Eastern Mediterranean.

The Samos earthquake expands our view of the effects of the slab back-roll and the southward retreat of the entire subduction system dominating the Aegean and western Anatolia tectonics. The extension is accommodated by opening parallel oriented grabens forming basins, such as the Samos-Ikaria basins and Buyuk-Menderes grabens (see Fig. 8). The Samos and Ikaria basins constitute two depocentres that should be jointly examined. The Samos sequence shows the interaction between the long-term evolution of the two basins (formed during the

old initiation of dextral transtension in the central Aegean) and active seismic faulting in the transtensional tectonic regime.

As an epilogue, the Samos sequence taught us, in the most dramatic way, that these basins can encompass strong ~Mw7 earthquakes. The hazard imposed to the urban regions across the eastern Aegean Sea is documented and joined cross-border efforts are needed to better understand the connection and continuation of the structures, especially in the offshore areas, that are less explored.

Data and Resources

Digital seismic waveforms were retrieved from the ORFEUS Eida-nodes (https://www.orfeus-eu.org/data/eida/nodes/), and AFAD (https://tadas.afad.gov.tr/event-detail/11995, log in as GUEST, and click the link again) and catalog and phase data are acquired from the following regional networks: HUSN (HL, doi:10.7914/SN/HL; HT, doi:10.7914/SN/HT; HA, doi:10.7914/SN/HA; HP, doi:10.7914/SN/HP; HI, doi:10.7914/SN/HI; HC, doi:10.7914/SN/HC); KOERI (KO, doi:10.7914/SN/KO), AFAD (TU, doi.org/10.7914/SN/TU) obtained through the web services of the individual networks and the corresponding EMSC-CSEM online services. Faults were obtained from the Greek Database of Seismogenic Sources (http://gredass.unife.it/, doi: 10.15160/unife/gredass/0200, the google map or KMZ file available through the "download GreDaSS" link). The code NonLInLoc used for the mainshock relocations is available at http://alomax.free.fr/nlloc/soft7.00/tar/NLL7.00_src.tgz. The StressInverse code, used in Fig. 8, is available at http://www.ig.cas.cz/en/stress-inverse/. Software ISOLA is available at http://geo.mff.cuni.cz/~jz/for_ISOLAnews/. The Linear Slip Inversion (LinSlipInv) method for kinematic slip inversions can be downloaded from http://fgallovic.github.io/LinSlipInv/. The ASTFs software is available at http://geo.mff.cuni.cz/~vp/ASTFs/. Full reference list of publications related to the Samos earthquake is available from International Seismological Centre, On-line Event Bibliography (http://www.isc.ac.uk/event_bibliography/eventindex.php). Some figures were drawn using the Generic Mapping Tools (GMT) software (Wessel & Smith, 1998).

Acknowledgments

We acknowledge the duty analysts in Greece and Turkey for the careful analysis of the data, staff members for maintenance and operation of the networks. We also thank our colleague A. Ganas for providing GNSS data before publication. AK and NV acknowledge support by the project "Safe-Schools" which is implemented under the Action "Reinforcement of the Research and Innovation Infrastructure", funded by the Operational Programme "Competitiveness, Entrepreneurship and Innovation" (NSRF 2014-2020) and co-financed by Greece and the EU (European Regional Development Fund). JZ and FG were supported by the Czech Science Foundation. E.S. and A.S acknowledge financial support by the HELPOS project, 'Hellenic Plate Observing System' (MIS

5002697).

References

Akyol, N., Zhu, L., Mitchell, B. J., Sözbilir, H., & Kekovalı, K. (2006). Crustal structure and local seismicity in western Anatolia. *Geophysical Journal International*, 166(3), 1259–1269. https://doi.org/10.1111/j.1365-246X.2006.03053.x

Beniest, A., Brub, J., Corini, C., Crombez, V., Deschamps, R., Hamon, Y., & Smit, J. (2016). Interaction between trench retreat and Anatolian escape as recorded by neogene basins in the northern Aegean Sea. Marine and Petroleum Geology, 77, 30-42.

Bertero, M., Bindi, D., Boccacci, P., Cattaneo, M., Eva, C., & Lanza, V. (1997). Application of the projected Landweber method to the estimation of the source time function in seismology. *Inverse Probl.*, 13, 465–486. doi: 10.1088/0266-5611/13/2/017.

Brun, J.-P., Faccenna, C., Gueydan, F., Sokoutis, D., Philippon, M., Kydonakis, K., & Gorini, C. (2016). The two-stage Aegean extension, from localized to distributed, a result of slab rollback acceleration. *Can. J. Earth Sci.*, 53, 1142-1157.

Calderoni, G., Rovelli, A., Ben-Zion, Y., & Di Giovambattista, R. (2015). Along-strike rupture directivity of earthquakes of the 2009 L'Aquila, central Italy seismic sequence. *Geophysical Journal International*, 203(1), 399–415. https://doi.org/10.1093/gji/ggv275

Cetin, K., Mylonakis, G., Sextos, A., Stewart, J., Akbaş, B., Akgün, M., et al. (2020). Seismological and Engineering Effects of the M 7.0 Samos Island (Aegean Sea) Earthquake. https://doi.org/10.18118/G6H088

Caputo, R., & Pavlides, S. (2013). The Greek Database of Seismogenic Sources (GreDaSS), Version 2.0.0: A compilation of potential seismogenic sources (M>5.5) in the Aegean region. doi:10.15160/unife/gredass/0200

Chatzipetros, A., Kiratzi, A., Sboras, S., Zouros, N., & Pavlides, S. (2013). Active faulting in the north-eastern Aegean Sea Islands. *Tectonophysics,* 597-598, 106-122. https://doi.org/10.1016/j.tecto.2012.11.026

Courboulex, F., Santoyo, M. A., Pacheco, J. F., & Singh, S. K. (1997). The September 14 1995 (M = 7.3) Copala, Mexico, earthquake: A source study using teleseismic, regional, and local data. *Bull. Seismol. Soc. Am.*, 87(4), 999–1010.

Chousianitis, K., & Konca, A. O. (2021). Rupture process of the 2020 Mw7.0Samos earthquake and its effect on surrounding active faults. *Geophysical Research Letters* 48: e2021GL094162. https://doi.org/10.1029/2021GL094162

Di Giacomo, D., Storchak, D. A., Safronova, N., Ozgo, P., Harris, J., Verney, R., & Bondár, I. (2014). A New ISC Service: The Bibliography of Seismic Events. *Seismol. Res. Lett.*, 85, 2, 354-360. doi: 10.1785/0220130143

Dogan, G.G., Yalciner, A.C., Yuksel, Y., Ulutaş, E., Polat, O., Güler, I., Şahin, C., Tarih, A., & Kânoğlu, U. (2021). The 30 October 2020 Aegean Sea Tsunami: Post-Event Field Survey Along Turkish Coast. *Pure Appl. Geophys.*, 178, 785–812. https://doi.org/10.1007/s00024-021-02693-3

Dziewonski, A. M., Chou, T.-A., & Woodhouse, J. H. (1981). Determination of earthquake source parameters from waveform data for studies of global and regional seismicity. *J. Geophys. Res.*, 86, 2825-2852. doi:10.1029/JB086iB04p02825

Ekström, G., Nettles, M., & Dziewonski, A. M. (2012). The global CMT project 2004-2010: Centroid-moment tensors for 13,017 earthquakes. *Phys. Earth Planet. Inter.*, 200-201, 1-9. doi:10.1016/j.pepi.2012.04.002

England, P., Houseman, G., & Nocquet, J.-M. (2016). Constraints from GPS measurements on the dynamics of deformation in Anatolia and the Aegean. *Journal of Geophysical Research: Solid Earth*, 121(12), 8888–8916. https://doi.org/10.1002/2016JB013382

Evelpidou, N., Karkani, A., & Kampolis, I. (2021). Relative sea level changes and morphotectonic implications triggered by the Samos earthquake of October 30 2020. *Journal of Marine Science and Engineering*, 9.

Faccenna, C., Becker, T.W., Auer, L., Billi, A., Boschi, L., Brun, J. P., Capitanio, F. A., Funiciello, F., Horvàth, F., Jolivet, L., Piromallo, C., Royden, L., Rossetti, F., & Serpelloni, E. (2014). Mantle dynamics in the Mediterranean. *Reviews of Geophysics*, 52(3), 283–332. https://doi.org/10.1002/2013RG000444.

Foumelis, M., Papazachos, C., Papadimitriou, E., Karakostas, V., Ampatzidis, D., Moschopoulos, G., Kostoglou, A., Ilieva, M., Minos-Minopoulos, D., Mouratidis, A., Kkallas, Ch., & Chatzipetros, A. (2021). On rapid multidisciplinary response aspects for Samos 2020 M7.0 Earthquake. *Acta Geophysica*, 69, 1025-1048. https://doi.org/10.1007/s11600-021-00578-6

Harris, D. XAPiir: A recursive digital filtering package. United States: N. p., 1990. Web. doi:10.2172/6416972

Hartzell, S. H. (1978). Earthquake aftershocks as Green's functions. *Geophys. Res. Lett.*, 5, 1–4, doi: 10.1029/GL005i001p00001.

Gallovič, F., & Zahradník, J. (2011). Toward understanding slip-inversion uncertainty and artifacts II: singular value analysis. *J. Geophys. Res.*, 116, B02309.

Gallovič, F. (2016). Modeling Velocity Recordings of the Mw 6.0 South Napa, California, Earthquake: Unilateral Event with Weak High-Frequency Directivity. *Seismological Research Letters*, 87(1), 2–14. https://doi.org/10.1785/0220150042

Gallovič, F., Imperatori, W., & Mai, P. M. (2015). Effects of three-dimensional crustal structure and smoothing constraint on earthquake slip inversions: Case

study of the Mw6.3 2009 L'Aquila earthquake. *Journal of Geophysical Research: Solid Earth*, 120(1), 428–449. https://doi.org/10.1002/2014JB011650

Gallovič, F., Valentová, Ľ., Ampuero, J.-P., & Gabriel, A.-A. (2019). Bayesian Dynamic Finite-Fault Inversion: 2. Application to the 2016 Mw6.2 Amatrice, Italy, Earthquake. *J. Geophys. Res. Solid Earth*, 124, 6970-6988.

Ganas, A., Elias, P., Briole, P., Tsironi, V., Escartin, J., Karasante, I., & Efstathiou, E. (2020). Fault responsible for Samos earthquake identified. *Temblor*, https://doi.org/10.32858/temblor.134

Ganas, A., Elias, P., Briole, P., Valkaniotis, S., Escartin, J., Tsironi, V., Karasante, I., & Kosma, C. (2021). Co-seismic and postseismic deformation, field observations and fault model of the October 30, 2020 Mw=7.0 Samos earthquake, Aegean Sea. *Acta Geophysica*, 69, 999-1024. https://doi.org/10.1007/s11600-021-00599-1

Jackson, J. (1987). Active normal faulting and crustal extension. In "Continental Extensional Tectonics", Coward, M.P., Dewey, J.F. & Hancock, P.L. (eds), Geological Society Special Publication No. 28, 3-17.

Jolivet, L., Menant, A., Sternai, P., Rabillard, A., Arbaret, L., Augier, R., Laurent, V., Beaudoin, A., Grasemann, B., Huet, B., Labrousse, L., & Laetitia le pourhiet (2015). The geological signature of a slab tear below the Aegean. *Tectonophysics*, 659. https://doi.org/10.1016/j.tecto.2015.08.004

Kalafat, D., Gürbüz, C., & Uçer, B. (1987). Investigation of the crust and upper mantle in the west of Turkey. *DepremArastirmaBulteni*, 14(59), 43–64.

Karabulut, H., Paul, A., Özbakır, A. D., Ergün, T., & Şentürk, S. (2019). A new crustal model of the Anatolia–Aegean domain: evidence for the dominant role of isostasy in the support of the Anatolian plateau. *Geophysical Journal International*, 218(1), 57–73. https://doi.org/10.1093/gji/ggz147

Karakostas, V., Tan, O., Kostoglou, A., Papadimitriou, E., & Bonatis, P. (2021). Seismotectonic implications of the 2020 Samos, Greece, Mw 7.0 mainshock based on high-resolution aftershock relocation and source slip model. *Acta Geophysica*, 69, 979-996, https://doi.org/10.1007/s11600-021-00580-y

Kaypak, B., & Gökkaya, G. (2012). 3-D imaging of the upper crust beneath the Denizli geothermal region by local earthquake tomography, western Turkey. *Journal of Volcanology and Geothermal Research*, 211–212, 47–60. https://doi.org/10.1016/j.jvolgeores.2011.10.006

Kiratzi, A., & Koskosidi, A. (2018). Constrains on the near-source motions of the Kos-Bodrum 20 July 2017 Mw6.6 earthquake. Conference: 16th European Conference on Earthquake Engineering at: Thessaloniki, Greece.

Kiratzi, A., Papazachos, C., Özacar, A., Pinar, A., Kkallas, Ch., & Sopachi, E. (2021). Characteristics of the 2020 Samos earthquake (Aegean Sea) using seismic data. *Bulletin of Earthquake Engineering*, DOI:10.1007/s10518-021-01239-1

Konca, A. O., Guvercin, S. E., Ozarpaci, S., Ozdemir, A., Funning, G. J., Dogan, U., Ergintav, S., Floyd, M., Karabulut, H., & Reilinger, R. (2019). Slip distribution of the 2017 Mw6.6 Bodrum–Kos earthquake: resolving the ambiguity of fault geometry. *Geophys. J. Int.*, 219 (2), 911–923.

Konstantinou, K. I. (2018). Estimation of optimum velocity model and precise earthquake locations in NE Aegean: Implications for seismotectonics and seismic hazard. *Journal of Geodynamics*, 121, 143–154. https://doi.org/10.1016/j.jog.2018.07.005

Laske, G., Masters, G., Ma, Z., & Pasyanos, M. (2013). Update on CRUST1.0 - A 1-degree Global Model of Earth's Crust. *In EGU General Assembly Conference Abstracts,* (pp. EGU2013-2658).

Lawson, C. L., & Hanson, R. J. (1974). Solving least squares problems. Prentice-Hall Series in Automatic Computation.

Lentas, K., Gkarlaouni, C. G., Kalligeris, N., & Melis, N. S. (2021). The October 30 2020, MW = 7.0, Samos earthquake: aftershock relocation, slip model, Coulomb stress evolution and estimation of shaking. *Bull. Earthquake Eng.*. https://doi.org/10.1007/s10518-021-01260-4

Le Pichon, X., Şengör, A. C., & İmren, C., (2019). A new approach to the opening of the eastern Mediterranean Sea and the origin of the Hellenic Subduction Zone. Part 1: The eastern Mediterranean Sea. *Can. J. Earth Sci.*, 56, 1119–1143.

Liu, J., & Zahradník, J. (2020). The 2019 MW 5.7 Changning earthquake, Sichuan Basin, China: A shallow doublet with different faulting styles. Geophysical Research Letters, 47, e2019GL085408. https://doi.org/10.1029/2019GL085408

Lomax, A., Virieux, J., Volant, P., & Berge-Thierry, C. (2000). Probabilistic Earthquake Location in 3D and Layered Models. In C. H. Thurber & N. Rabinowitz (Eds.), Advances in Seismic Event Location (pp. 101–134). *Dordrecht: Springer Netherlands.* https://doi.org/10.1007/978-94-015-9536-0_5

López-Comino, J. A., & Cesca, S. (2018). Source complexity of an injection induced event: The 2016 Mw 5.1 Fairview, Oklahoma earthquake. *Geophys. Res. Lett.*, 45,4025–4032. https://doi.org/10.1029/2018GL077631

Makra, K., Rovithis, E., Riga, E., Raptakis, D., & Pitilakis, K. (2021). Amplification features and observed damages in İzmir (Turkey) due to 2020 Samos (Aegean Sea) earthquake: identifying basin effects and design requirements. *Bulletin of Earthquake Engineering*, 19(12), 4773-4804.

McGuire, J. J. (2004). Estimating finite source properties of small earthquake ruptures. *Bull. Seismol. Soc. Am.,* 94, 377–393, doi: 10.1785/0120030091

Meng, J., Sinoplu, O., Zhou, Z., Tokay, B., Kusky, T., Bozkurt, E., & Wang, L. (2021). Greece and Turkey Shaken by African tectonic retreat. *Scientific Reports*, 11(1), 6486. https://doi.org/10.1038/s41598-021-86063-y

Mori, J., & S. Hartzell (1990). Source inversion of the 1988 Upland, California, earthquake: Determination of a fault plane for a small event. *Bull. Seismol. Soc. Am.*, 80, 507–518.

Mueller, C. S. (1985). Source pulse enhancement by deconvolution of an empirical Green's function. *Geophys. Res. Lett.*, 12, 33–36, doi: 10.1029/GL012i001p00033.

Nomikou, P., Evangelidis, D., Papanikolaou, D., Lampridou, D., Litsas, D., Tsaparas, Y., & Koliopanos, I. (2021). Morphotectonic Analysis along the Northern Margin of Samos Island, Related to the Seismic Activity of October 2020, Aegean Sea, Greece. *Geosciences*, 11(2). https://doi.org/10.3390/geosciences11020102

Novotný, O., Zahradník, J., & Tselentis, G.-A. (2001). Northwestern Turkey Earthquakes and the Crustal Structure Inferred from Surface Waves Observed in Western Greece. *Bull. Seismol. Soc. Am.*, 91(4), 875–879. https://doi.org/10.1785/0120000116

Özer, Ç., & Polat, O. (2017). 3-D crustal velocity structure of Izmir and surroundings. *Journal of the Faculty of Engineering and Architecture of Gazi University*, 32 (3), 733-747.

Özer, Ç., Gök, E., & Polat, O. (2018). Three-Dimensional Seismic Velocity Structure of the Aegean Region of Turkey from Local Earthquake Tomography. *Annals of Geophysics*, 61. https://doi.org/10.4401/ag-7543

Pacor, F., Gallovič, F., Puglia, R., Luzi, L., & D'Amico, M. (2016). Diminishing high-frequency directivity due to a source effect: empirical evidence from small earthquakes in the Abruzzo region, Italy. *Geophys. Res. Lett.*, 43, 5000-5008.

Papadimitriou, P., Kapetanidis, V., Karakonstantis, A., Spingos, I., Kassaras, I., Sakkas, V., Kouskouna, V., Karatzetzou, A., Pavlou, K., Kaviris, G., & Voulgaris, N. (2020). First Results on the Mw=6.9 Samos Earthquake of October 30 2020. *Bulletin Geological Society of Greece*, 56, 251-279.

Pasyanos, M. E., Walter, W. R., Flanagan, M. P., Goldstein, P., & Bhattacharyya, J. (2004). Building and Testing an a priori Geophysical Model for Western Eurasia and North Africa. Pure and Applied Geophysics, 161(2), 235–281. https://doi.org/10.1007/s00024-003-2438-5

Philippon, M., Brun, J.-P., & Gueydanc, F. (2012). Deciphering subduction from exhumation in the segmented Cycladic Blueschist Unit (Central Aegean, Greece). *Tectonophysics*, 524-525, 116-134. doi:10.1016/j.tecto.2011.12.025

Pizzi, A., Di Domenica, A., Gallovič, F., Luzi, L., & Puglia, R. (2017). Fault segmentation as constraint to the occurrence of the main shocks of the 2016 Central Italy seismic sequence. *Tectonics*, 36, 2370-2387.

Taymaz, T., Yolsal-Çevikbilen, S., Irmak, T. S., Vera, F., Liu, Ch., Eken, T., Zhang, Z., Erman, C., & Keleş, D. (2022). Kinematics of the 30 October 2020

Mw 7.0 Néon Karlovásion (Samos) earthquake in the Eastern Aegean Sea: Implications on source characteristics and dynamic rupture simulations, Tectonophysics, 229223.

Roumelioti, Z., Benetatos, C., & Kiratzi, A. (2009). The February 14 2008 earthquake (M6.7) sequence offshore south Peloponnese (Greece): Source models of the three strongest events. *Tectonophysics*, 471, 272–284. https://doi.org/10.1016/j.tecto.2009.02.028

Sengor, A.M.C., Tüysüz, O., Imren, C., Sakınç, M., Eyidogan, H., Görür, N., Le Pichon, X., & Rangin, C. (2005). The North Anatolian Fault. A new look: *Annu. Rev. Earth Planet. Sci*, 33: 37–112. doi: 10.1146/annurev.earth.32.101802.120415

Sakellariou, D., Mascle, J., & Lykousis, V. (2013). Strike slip tectonics and transtensional deformation in the Aegean region and the Hellenic arc: Preliminary results. *Bulletin of the Geological Society of Greece*, 47. doi: 10.12681/bgsg.11098

Sokos, E., Kiratzi, A., Gallovič, F., Zahradník, J., Serpetsidaki, A., Plicka, V., Janský, J., Kostelecký, J., & Tselentis, G.-A. (2015). Rupture process of the 2014 Cephalonia, Greece, earthquake doublet (Mw6) as inferred from regional and local seismic data. *Tectonophysics*, 656, 131-141.

Sokos, E., Zahradník, J., Gallovič, F., Serpetsidaki, A., Plicka, V., & Kiratzi, A. (2016). Asperity break after 12 years: The Mw6.4 2015 Lefkada (Greece) earthquake. *Geophys. Res. Lett.*, 43, 6137-6145.

Sokos, E., Gallovič, F., Evangelidis, C. P., Serpetsidaki, A., Plicka, V., Kostelecký, J., & Zahradník, J. (2020). The 2018 Mw 6.8 Zakynthos, Greece, Earthquake: Dominant Strike-Slip Faulting near Subducting Slab. *Seismological Research Letters*, 91(2A), 721–732. https://doi.org/10.1785/0220190169

Triantafyllou, I., Gogou, M., Mavroulis, S., Lekkas, E., Papadopoulos, G.A., & Thravalos, M. (2021). The Tsunami Caused by the October 30 2020 Samos (Aegean Sea) Mw7.0 Earthquake: Hydrodynamic Features, Source Properties and Impact Assessment from Post-Event Field Survey and Video Records. *J. Mar. Sci. Eng.*, 9, 68. https://doi.org/10.3390/jmse9010068

Vallée, M. (2004). Stabilizing the empirical Green function analysis: Development and the projected Landweber method. *Bull. Seismol. Soc. Am.*, 94, 394–409, doi: 10.1785/0120030017

Vallée, M., Charléty, J., Ferreira, A. M. G., Delouis, B., & Vergoz, J. (2011). SCARDEC: a new technique for the rapid determination of seismic moment magnitude, focal mechanism and source time functions for large earthquakes using body-wave deconvolution. *Geophysical Journal International*, 184(1), 338–358. https://doi.org/10.1111/j.1365-246X.2010.04836.x

Waldhauser, F., & Ellsworth, W. L. (2000). A Double-difference Earthquake location algorithm: Method and application to the Northern Hayward Fault,

California. *Bull. Seismol. Soc. Am.*, 90(6), 1353–1368. https://doi.org/10.1785/0120000006

Waldhauser, F. (2001). hypoDD--A program to compute double-difference hypocenter locations. Open-File Report. doi:10.3133/ofr01113

Wessel, P., & Smith, W. H. F. (1998). New, improved version of generic mapping tools released. *Eos Transactions American Geophysical Union*, 79(47), 579–579. https://doi.org/10.1029/98EO00426

Zahradník, J., & Gallovič, F. (2010). Toward understanding slip-inversion uncertainty and artifacts, J. Geophys. Res., 115, B09310.

Zahradník, J., & Sokos, E. (2014). The M w 7.1 Van, Eastern Turkey, earthquake 2011: two-point source modelling by iterative deconvolution and non-negative least squares. *Geophysical Journal International*, 196(1), 522–538.

Zahradník, J., & Sokos, E. (2018). ISOLA Code for Multiple-Point Source Modeling—Review. In S. D'Amico (Ed.), Moment Tensor Solutions: A Useful Tool for Seismotectonics (pp. 1–28). *Cham: Springer International Publishing.* https://doi.org/10.1007/978-3-319-77359-9_1

Zúñiga, F. R, & Tan, O. (2021). Introduction to the special issue on the October 30, 2020, Mw7.0, Samos Island, Greece, earthquake. *Acta Geophysica*, 69, 975–977. https://doi.org/10.1007/s11600-021-00612-7

List of Tables

Table 1

Mainshock hypocenter parameters as obtained from P- and S-wave arrivals benchmarking different velocity models within NonLinLoc code. 'Depth' is the formal, best-fitting value. For uncertainty, see Figure 2. The location provided by EMSC is listed for comparison.

Velocity Model	Origin Time (HH:MM:SS)	Latitude °N	Longitude °E	Depth (km)
Akyol et al., 2006	:51:25.10			
Konstantinou, 2018	:51:24.28			
Novotný et al., 2001	:51:25.15			
Özer and Polat, 2017	:51:24.51			
Özer et al., 2018	:51:23.64			
Crust1.0	:51:24.71			

Velocity Model	Origin Time (HH:MM:SS)	Latitude °N	Longitude °E	Depth (km)
EMSC	:51:25.70			

Table 2

Moment tensor solution for the mainshock calculated here alongside published ones (the letter f next to the depth value, H, denotes that it was fixed during the inversion).

Centroid Time hh:mm:ss	Centroid location Lat °N Lon °E	Hd (km)	Mo (Nm) ×e19	M_w	Nodal Plane 1 (Fault Plane)		Nodal Plane 2		slip vector (NP1)		Reference	
					strike°	dip°	rake°	strike°	dip°	rake°	az°/plunge°	
:51:37											/49	This study
:51:44			12f								/29	USGS
:51:26											/32	IPGP
:51:34			12f								/37	GCMT
:51:26											/37	INGV
:51:26				--							/45	OCA
:51:24											/46	AFAD
:51:27											/48	GFZ
:51:26											/49	UOA
:51:24											/47	NOA
:51:27											/55	KOERI

Table 3

Geometry of the fault considered in the finite-fault inversion and main characteristics of the inferred rupture model.

Parameter	Value
Seismic Moment	4e19Nm (constrained from GCMT)
Moment magnitude, M	7.0 (constrained from GCMT)
Fault length × width	100 km x 24 km
Strike/dip/rake of the fault (dips to N)	265°/40°/-110°
Fault center coordinates	37.899°N, 26.589°E
Fault top depth	0 km

Parameter	Value
Fault bottom depth	13 km
Rupture propagation	Unconstrained
Average displacement along the ruptured area	1.2 m
Maximum displacement	2.4 m
Ruptured area (slip > 0.2 m)	60 km x 20 km

List of Figures

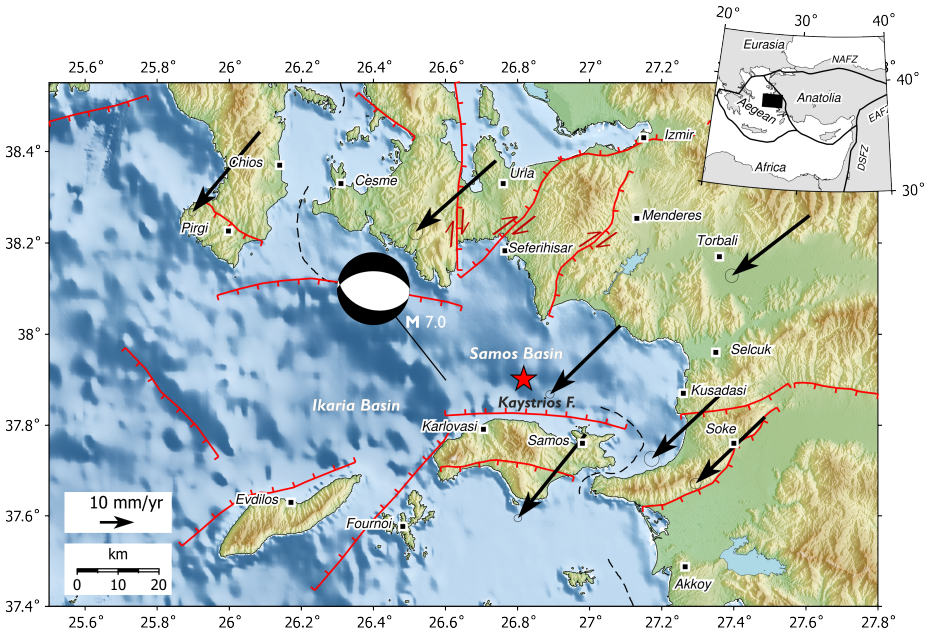

Figure 1. Epicenter location (star) and centroid moment tensor solution (beach-ball) of the Samos 2020 M7 earthquake, alongside active faults (red lines; from Caputo and Pavlides, 2013) and GPS-derived horizontal velocity vectors (black arrows; data from England et al., 2016). The study area within the broader tectonic context is shown in the inset (NAFZ: North Anatolian Fault Zone; EAFZ: East Anatolian Fault Zone; DSFZ: Dead Sea Fault Zone).

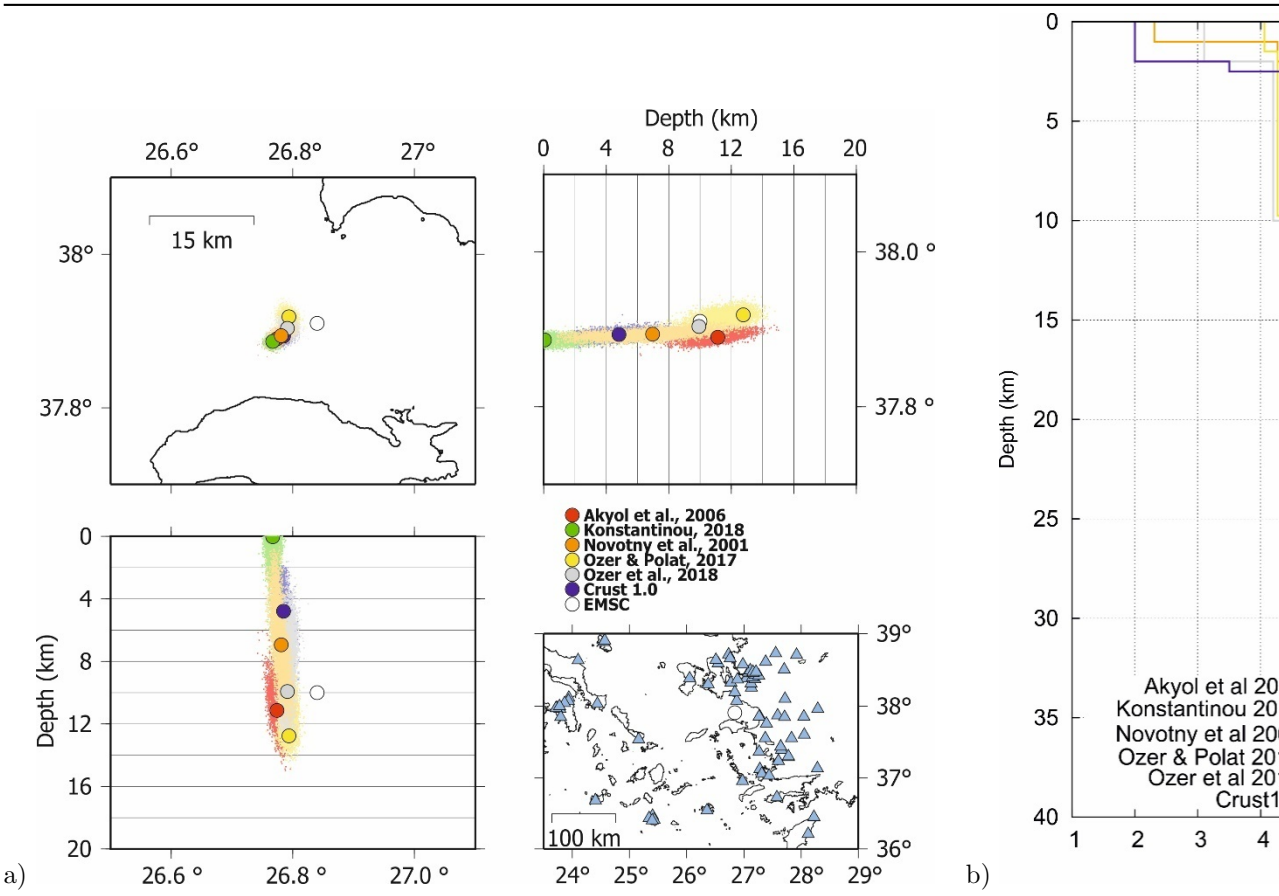

Figure 2. Relocation of mainshock hypocenter: a) Best-fit NonLinLoc solutions (circles) and their uncertainties (colored cloud-dots) obtained from the inversion of P- and S- phase arrivals at the stations (shown by gray triangles). b) The different velocity models explored. The Crust1.0 model is sampled at latitude = 37.5°N and longitude = 26.5°E. All models provide stable epicenter position ±2.5 km and shallow (<12 km) depth. Inverting P-phases only gives comparable results.

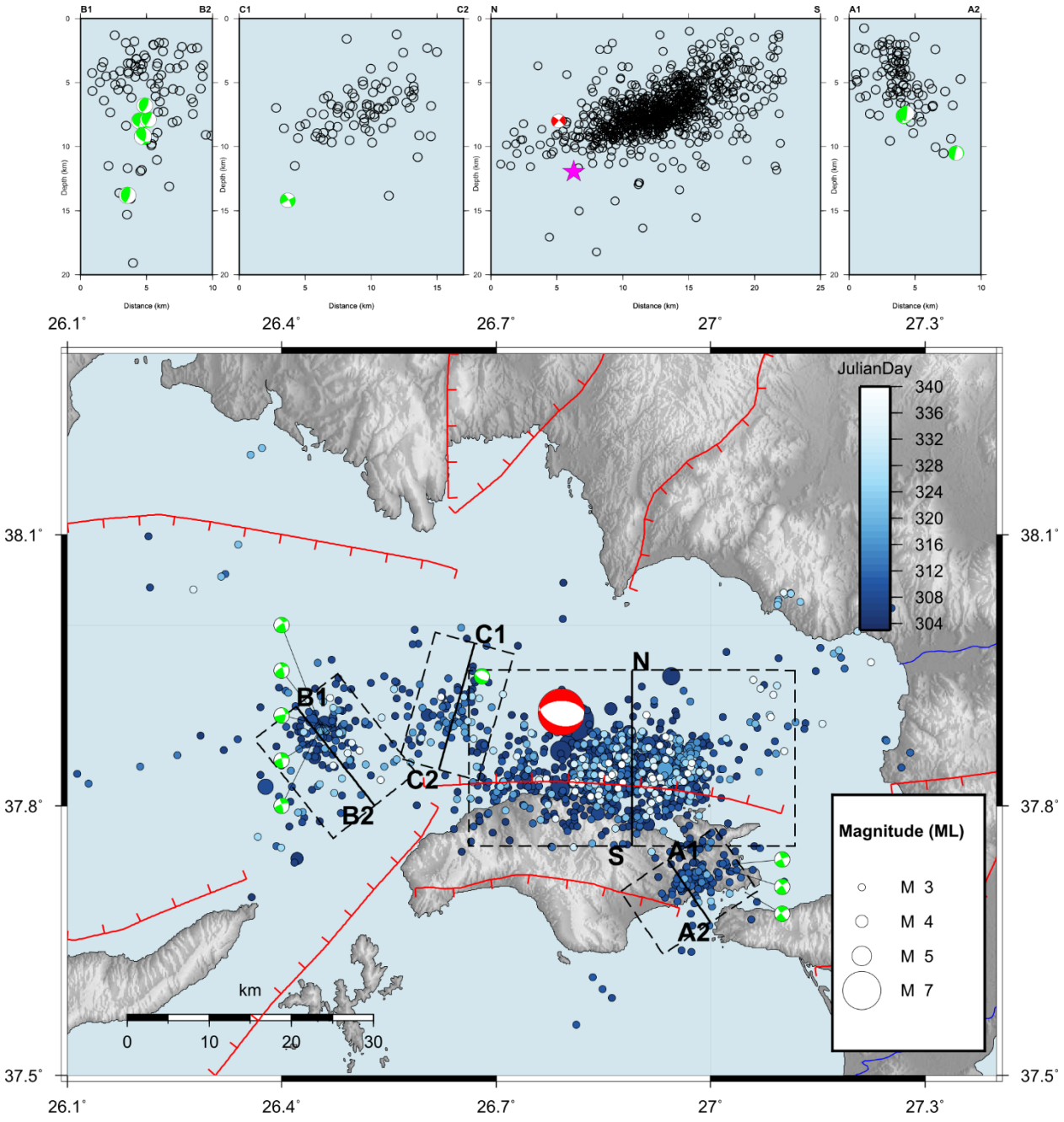

Figure 3. Spatial distribution of relocated aftershocks of the period October 30 to December 4, 2020, and designated cross-sections (top panels). Red beach ball represents the moment tensor solution of the mainshock, herein calculated, while green beach balls denote selected aftershock moment tensors from Karakostas

et al. (2021).

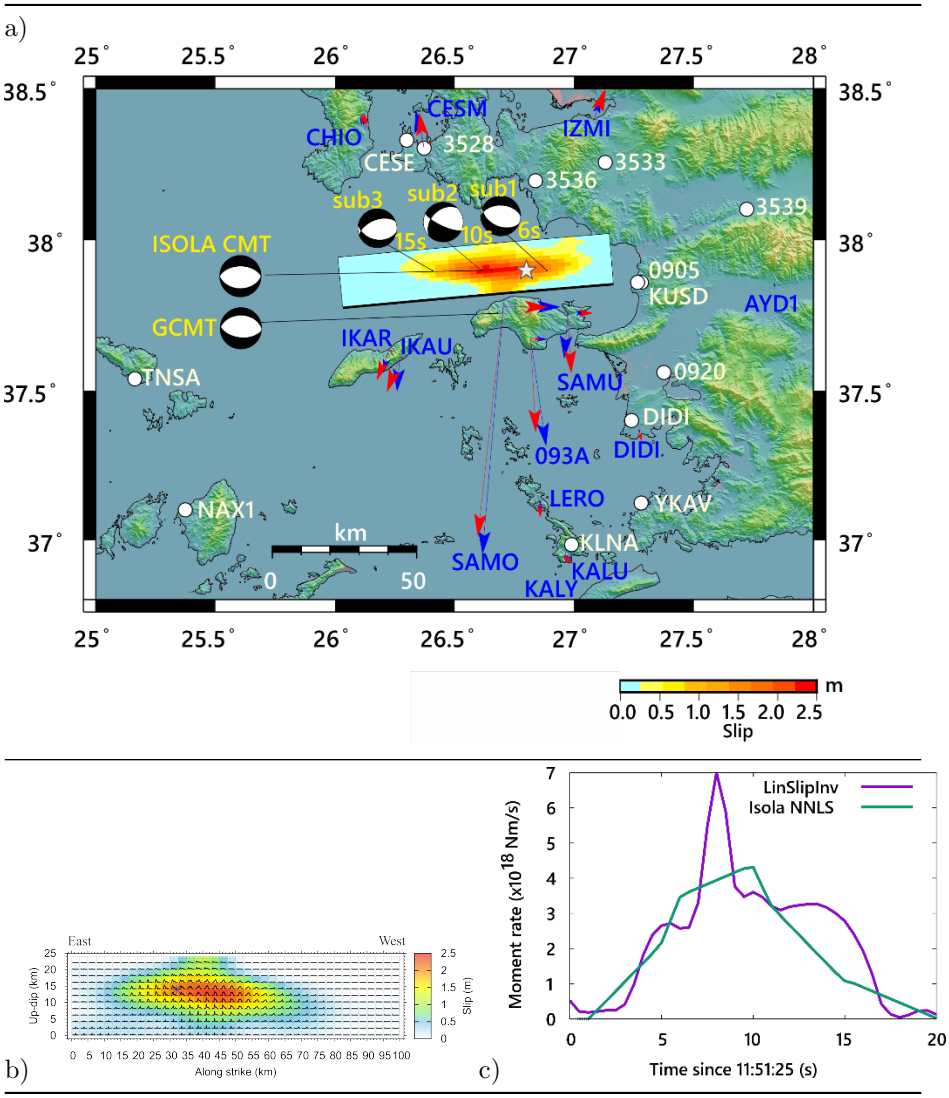

Figure 4. a) Map view of slip distribution (color-coded) from the LinSlipInv kinematic slip inversion on north-dipping fault (rectangle). Star is the preferred epicenter. Circles show strong motion stations used in the inversion. Arrows show GNSS daily solutions (blue) and the respective synthetic displacements (red); vertical (upward) motions are formally plotted as eastward arrows for clarity. Maximum horizontal displacement 35.7 cm was measured at the SAMO station. Multiple-point source model (sub 1,2,3) is shown by small beach balls, with depicted timing after the origin time. Isola CMT and GCMT solutions

are shown for reference. b) Cross section of slip model shown in a) with slip rate functions superimposed (maximum scaled to 0.5 m/s). c) Moment rate functions from LinSlipInv and Isola NNLS, depicting the source duration of ~20 s.

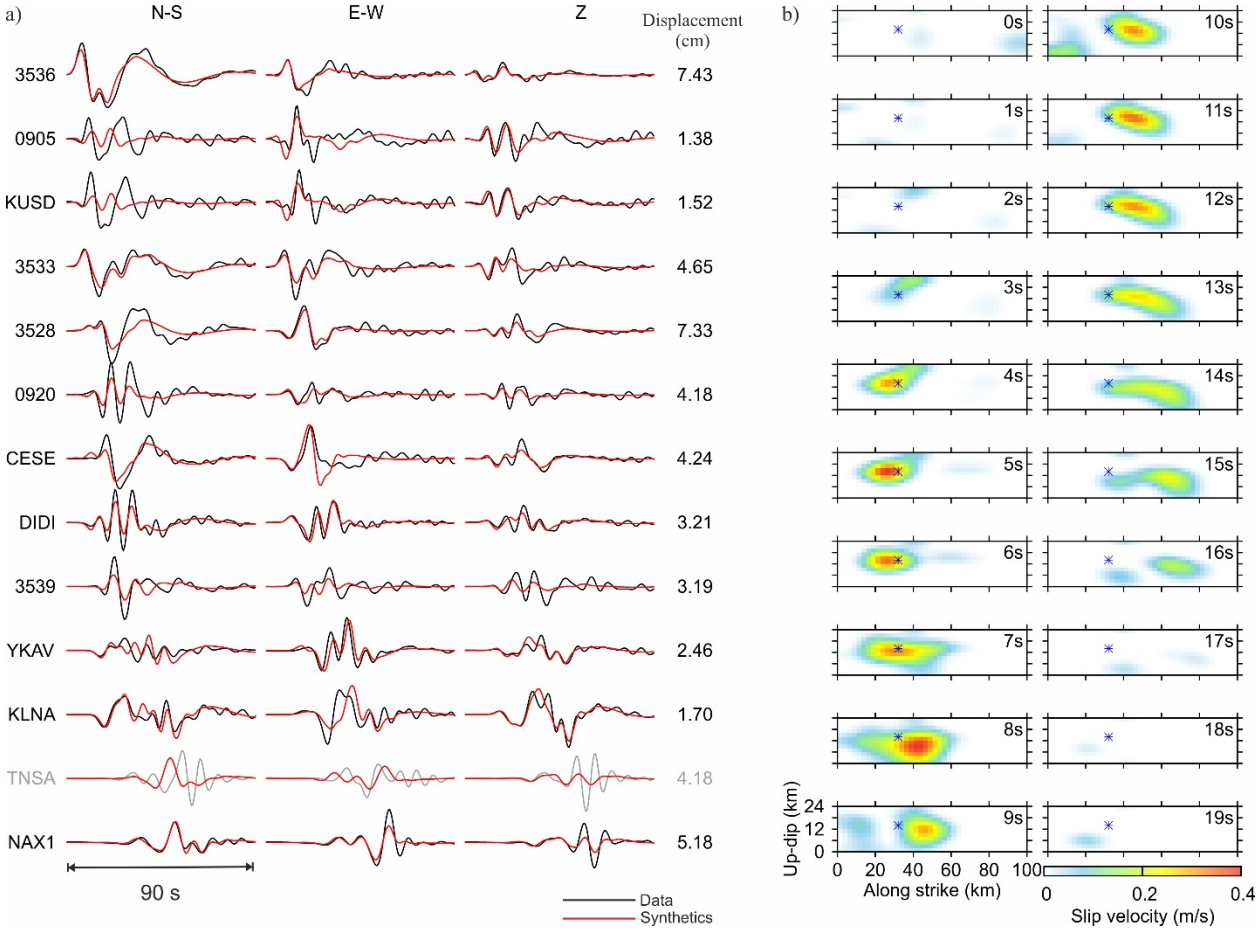

Figure 5. a) Waveform fit of displacement recordings in a in a frequency range of 0.02-0.15 Hz. The waveform in grey was not used in the inversion. b) Slip rate snapshots of our preferred rupture model inferred by the LinSlipInv kinematic inversion method (Fig. 4).

a) b)

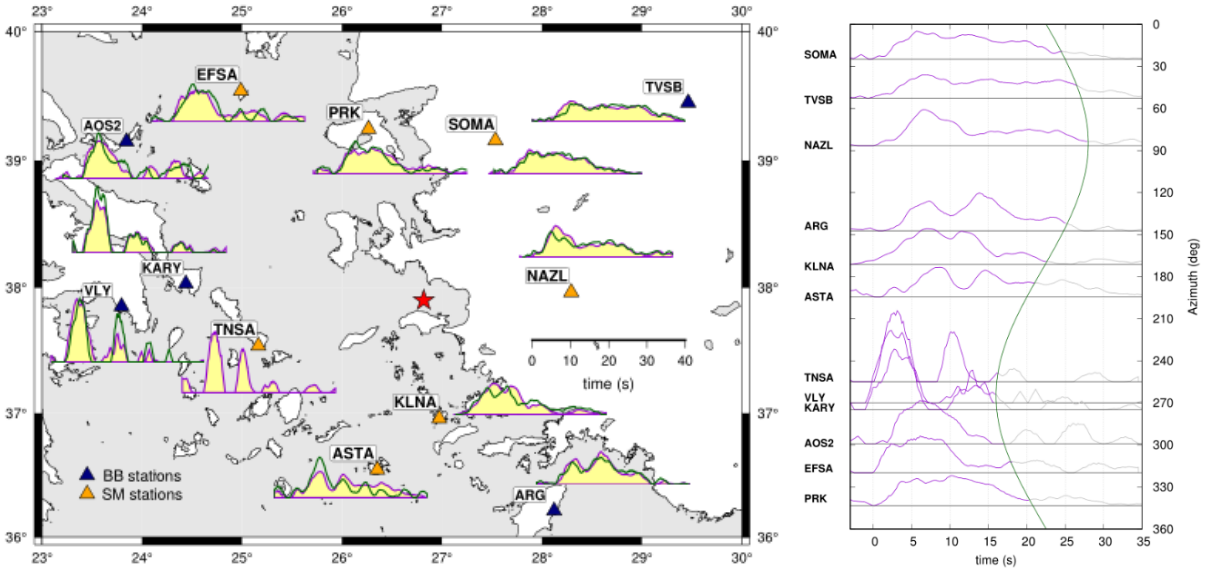

Figure 6. Apparent source time functions (ASTFs) obtained from the EGF method at regional broadband (blue triangles) and strong motion (orange triangles) stations in a) a map view and b) as a function of azimuth (for simplicity, only event 1 is drawn). The red star denotes the epicenter. Magenta and green ASTFs in panel a) are obtained from event1 and 2, respectively. Station TNSA has data just for event 1. Narrow and high amplitudes of ASTFs confirm the westward rupture propagation at western stations (KARY, VLY, TNSA) in contrast to longer duration and smaller amplitudes at the rest of the stations. The green curve line depicts the theoretical variation of the apparent duration for the rupture azimuth of 265 $^{\circ}$, total rupture duration of 22 s, and 7 s long westward-directive rupture propagation.

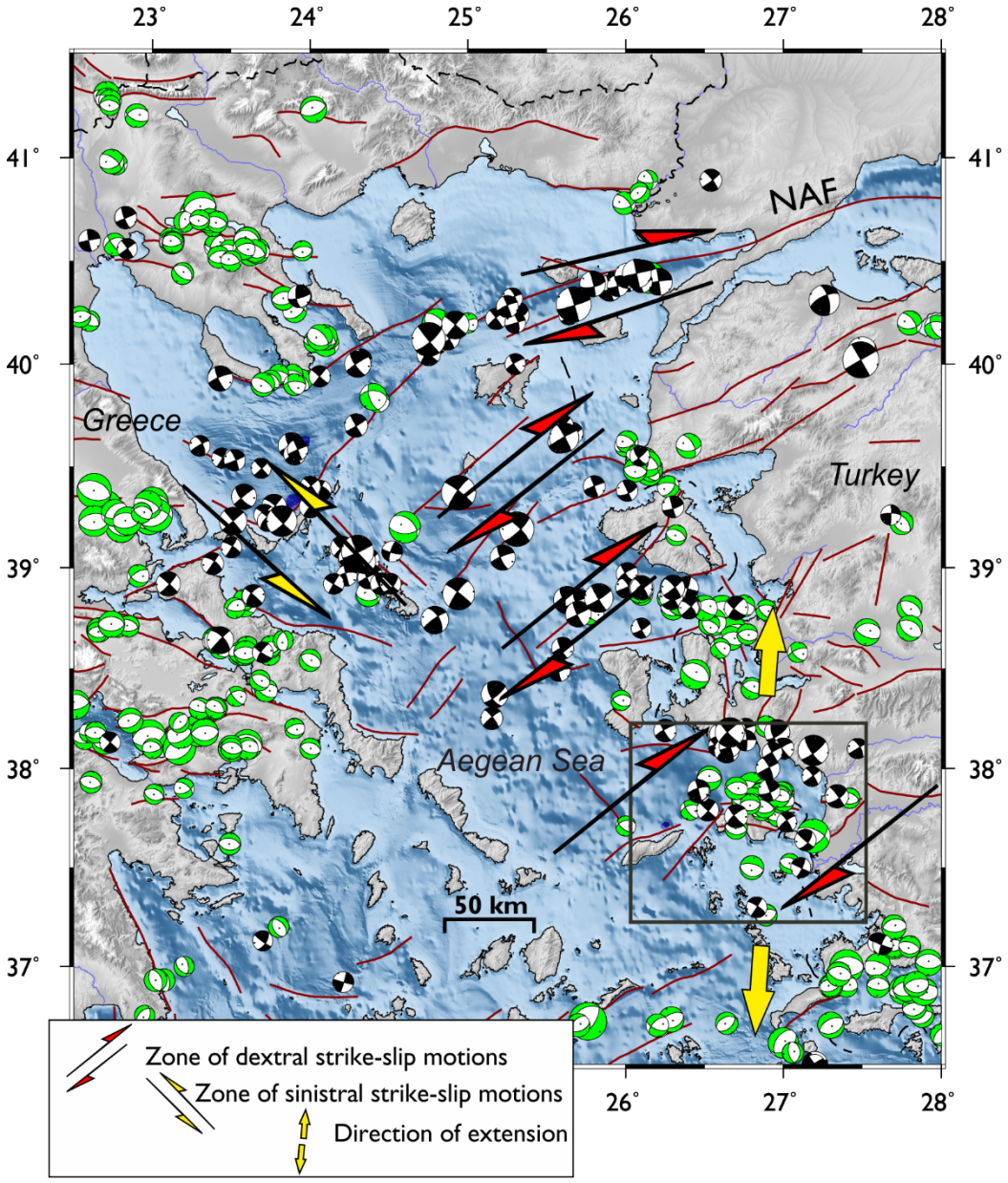

Figure 7. Shear motions within the Aegean Sea, as depicted by earthquake focal mechanisms (beach-balls: green= normal faulting; black=strike-slip faulting; M>=4.0). Dextral motions are imposed from the North Anatolian Fault as it splays into en-echelon NE-SW dextral strike-slip faults and associated grabens (pull-apart structures) in the Aegean Sea, terminating close to the eastern Greek coastline, along an NW-SE trending zone of sinistral strike-slip motions. (NAF:

North Anatolian Fault). Note the diminish of shear motions south of ~37.5°N parallel. The rectangle encloses the area analyzed in Figure 8, while the divergent arrows above and below the rectangle denote the direction of extension.

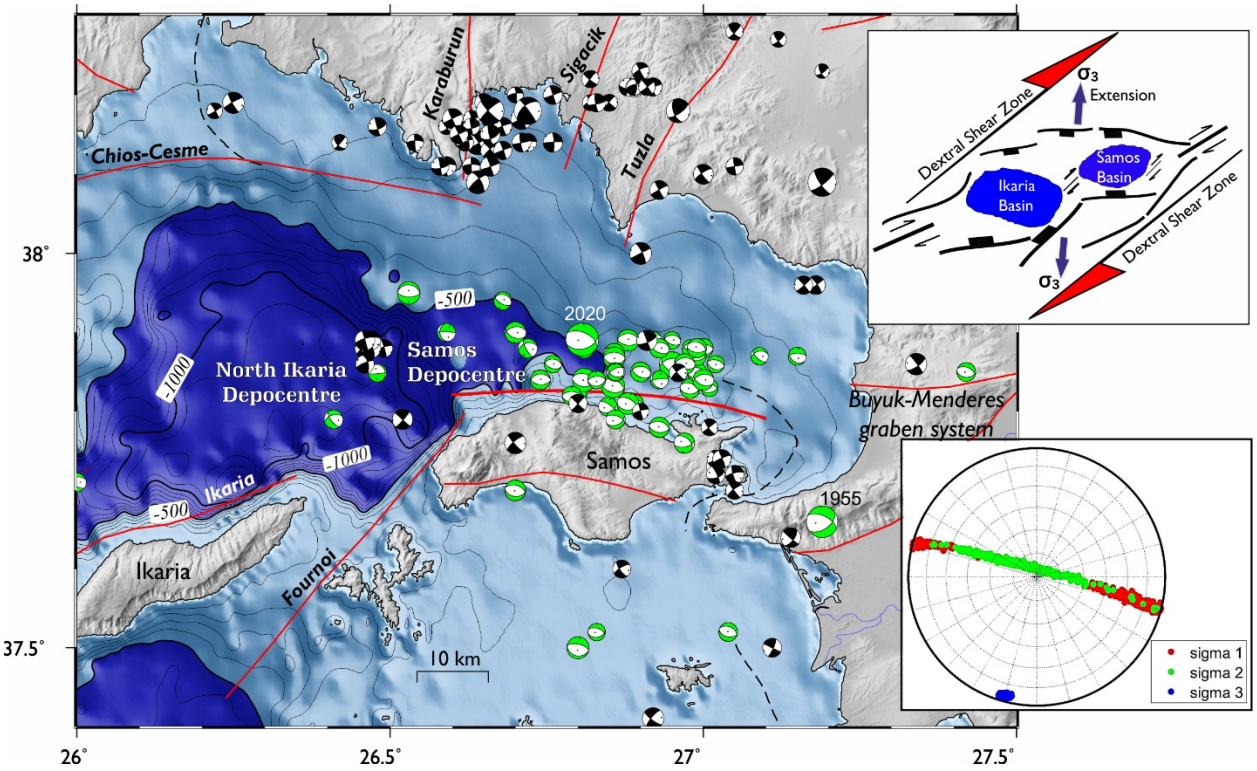

Figure 8: Close-up of our study area to show how the Samos event nicely fits the regional transtensional tectonics, with the evolution of two depocentres: the North Ikaria Depocentre and the Samos Depocentre. The former is a wide asymmetric deep (~1400 m) depression, while the latter is a smaller and considerably shallower (~690 m) depression. The focal mechanisms (beach-balls) show prevalence of ~E-W trending normal faulting (green), and the reactivation of older NW-SE and NE-SW structures, as strike-slip faults (black), all operating under an extensional stress field. Upper Inset: Simplified sketch to show the tectonic model for the Ikaria-Samos Basins developed along strike-slip faulting and oblique rifting: they are bounded by major en-echelon arranged faults. The direction of the extension ~N12°E as calculated from the sequence's focal mechanisms (direction of axis 3, lower inset), in good agreement with the broader stress field, is oblique to the axis of shearing, clearly depicting the evolution of basins (Samos and Ikaria Basins) within a rather oblique transtensional regime.

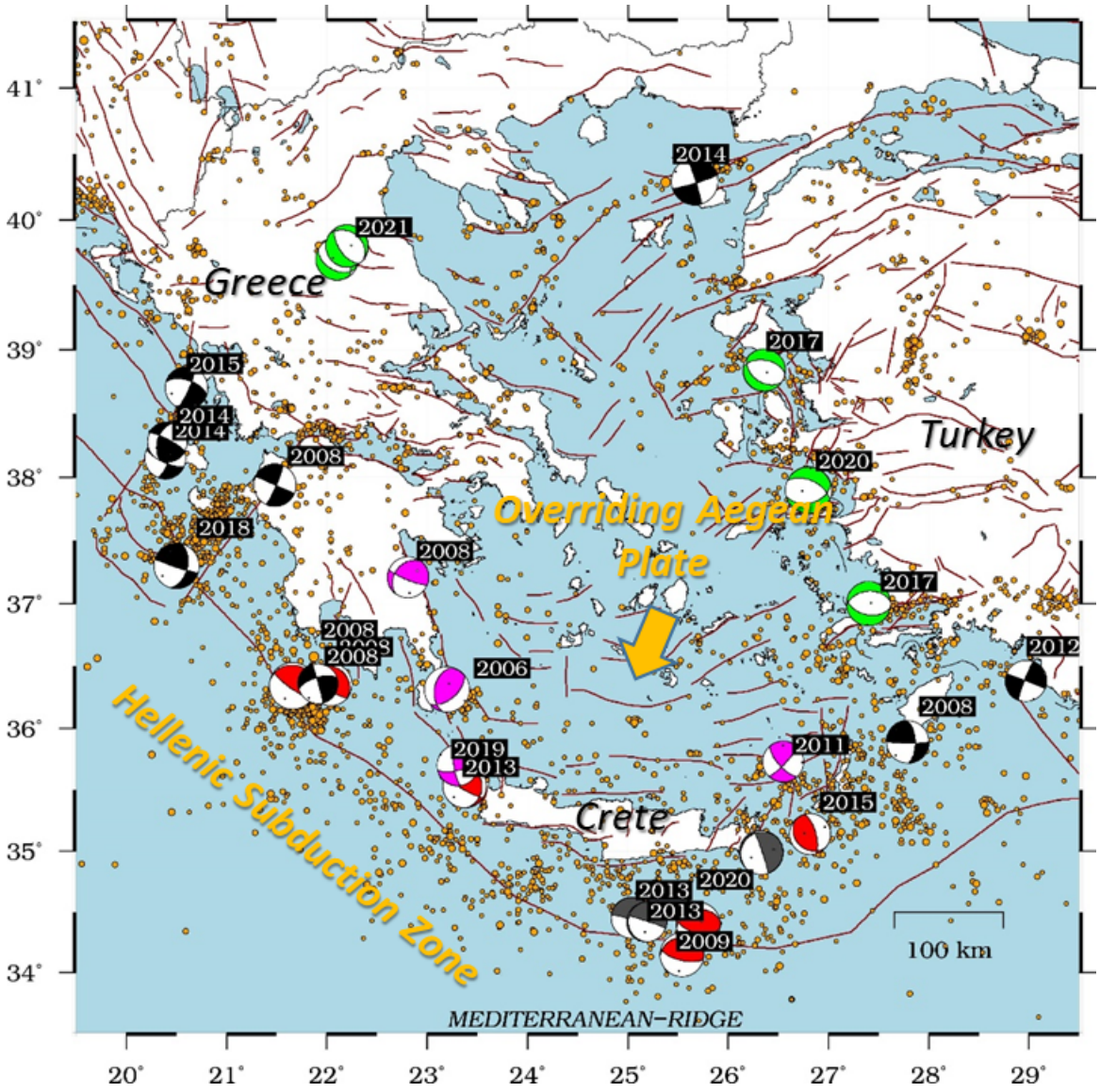

Figure 9. Localized signals of deformation: Focal mechanisms (beach balls) of a cascade of 27 strong Mw 6 earthquakes in the Aegean Sea and the surrounding lands during the last 15 years (2006 to 2021), and distribution of background seismicity (M > 4; orange circles) for the same period. Magenta beach-balls depict intermediate depth (h > 60km) events. The remaining ones are shallow, colored red for reverse/thrusts, green for normal faulting, black for strike-slip, and grey for unclassified faulting (three cases near Crete Island). This handful of focal mechanisms depicts all types of deformation of the area: compression along the subduction and within the subducting plate, extension and shear motions

along the overriding Aegean plate.